

Anil Yuksel

Department of Mechanical Engineering, The University of Texas at Austin, Austin, TX 78712

Edward T. Yu

Department of Electrical and Computer Engineering, The University of Texas at Austin, Austin, TX 78758

Michael Cullinan

Department of Mechanical Engineering, The University of Texas at Austin, Austin, TX 78712

Jayathi Murthy

Henry Samueli School of Engineering and Applied Science, University of California, Los Angeles, CA 90095

Thermal Transport in Nanoparticle Packings Under Laser Irradiation

Nanoparticle heating due to laser irradiation is of great interest in electronic, aerospace, and biomedical applications. This paper presents a coupled electromagnetic-heat transfer model to predict the temperature distribution of multilayer copper nanoparticle packings on a glass substrate. It is shown that heat transfer within the nanoparticle packing is dominated by the interfacial thermal conductance between particles when the interfacial thermal conductance constant, G_{IC} , is greater than $20\,\mathrm{MW/m^2K}$, but that for lower G_{IC} values, thermal conduction through the air around the nanoparticles can also play a role in the overall heat transfer within the nanoparticle system. The coupled model is used to simulate heat transfer in a copper nanoparticle packing used in a typical microscale selective laser sintering (μ -SLS) process with an experimentally measured particle size distribution and layer thickness. The simulations predict that the nanoparticles will reach a temperature of $730 \pm 3\,\mathrm{K}$ for a laser irradiation of $2.6\,\mathrm{kW/cm^2}$ and $1304 \pm 23\,\mathrm{K}$ for a laser irradiation of $6\,\mathrm{kW/cm^2}$. These results are in good agreement with the experimentally observed laser-induced sintering and melting thresholds for copper nanoparticle packing on glass substrates. [DOI: 10.1115/1.4045731]

Keywords: near-field thermal energy, interfacial thermal conductance, nanoparticle packings

1 Introduction

Thermal transport at the micro/nanoscale has attracted considerable interest due to scaling down of electronic device dimensions and the corresponding dramatic increase in power density. Concurrently, a growing trend in electronics is to integrate, monolithically, multiple functionalities via three-dimensional (3D) electronic packaging, but current fabrication techniques for such structures remain an outstanding challenge [1,2]. To overcome these challenges, a new microscale selective laser sintering (μ -SLS) technique has recently been suggested to create 3D metal structures with micron-scale features [3]. In this process, laser energy is applied, via a micromirror-array optical system, to a micron-thick layer of nanoparticles spread on a substrate to sinter the nanoparticles into a desired pattern. The process of adding a new layer of nanoparticles onto a sintered layer is continued until the full structure is built up.

Application of laser energy to micro/nanostructures results in thermal energy transport at micro/nanolength scales, and an understanding of laser/material interactions at these scales is vital. Due to the current lack of understanding of the laser/nanoparticle interactions that underlie the μ -SLS process, an iterative trial-anderror experimental process is generally used to determine the important process parameters that affect part quality. For example, laser properties such as fluence/intensity affect thermal transport within the micro/nanostructures, and different laser types such as femtosecond, nanosecond, or continuous wave lasers with different laser fluences have been investigated for various applications [4-7]. Indeed, laser/nanoparticle interactions create many challenges in understanding thermal transport in the micro/nanoscale regime, as the characteristic mean free paths of heat carriers may be comparable to the characteristic dimensions of the system, and the characteristic energy time-scale may be comparable to the characteristic times for energy carrier movement. Thus, the

Contributed by the Heat Transfer Division of ASME for publication in the JOURNAL OF HEAT TRANSFER. Manuscript received January 14, 2019; final manuscript received December 2, 2019; published online January 13, 2020. Assoc. Editor: Thomas Beechem.

traditional macro scale heat transfer analysis approach may not be applicable for the quantitative analysis of the μ -SLS process.

Furthermore, micro/nanometal particles employed in μ -SLS exhibit unique thermal and optical properties compared to the corresponding bulk properties, which can be engineered by appropriately tuning their structure [8–10]. For example, due to surface plasmon polariton excitations—collective motions of excited electrons within the metal nanoparticles that are coupled to the electromagnetic field-strong near-field scattering and confinement have been observed when metal nanoparticles are closely spaced each other [11-15]. This nonlocal and highly confined energy transport, which is created by electromagnetic waves, leads to changes in the thermal behavior of the nanostructure medium and creates "hot spots." This occurs when metal nanoparticle properties such as nanoparticle size and spacing are tuned due to sizedependent and frequency-dependent interactions with the incoming laser energy excitation. These interactions affect the optical properties of the metal nanoparticles, such as absorption, as well as the penetration depth for heating within the nanoparticle packings. In addition, pulsed laser excitation can influence thermal transport and the resulting temperature distribution within a nanoparticle packing due to the time required for equilibration between electron and lattice temperatures [16–18]. If the time required for the electron and lattice temperatures to equilibrate is longer than the laser pulse width, thermal equilibrium no longer applies. The electron and lattice temperatures need to be analyzed separately and need to be coupled with a defined coupling factor. A twotemperature model is commonly used to analyze such thermal transport in metal nanoparticles [19-21]. When the laser pulse duration is much longer than the electron-phonon relaxation time, and carrier mean free path is much smaller than the particle dimension, the diffusion equation can be applied for thermal transport analysis [22,23].

Within the nanoparticle packing, interfacial thermal conductance between the particles becomes one of the key parameters that characterize thermal transport. Interfacial thermal conductance, also known as *Kapitza* resistance, contributes to increased thermal resistance between the nanoparticles [24,25]. Thus, interfacial thermal conductance, which includes effects of interfacial

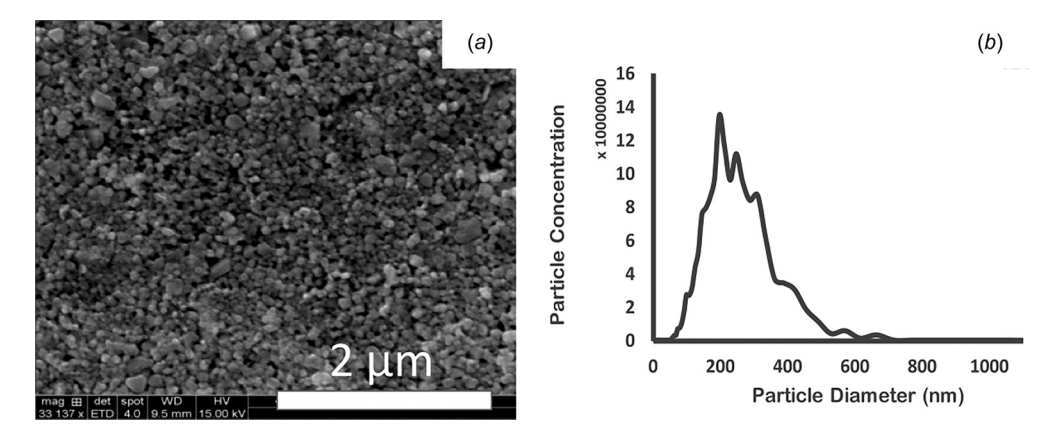


Fig. 1 (a) SEM image of the nanoparticle packing in an ink and (b) particle size distribution measured using dynamic light scattering

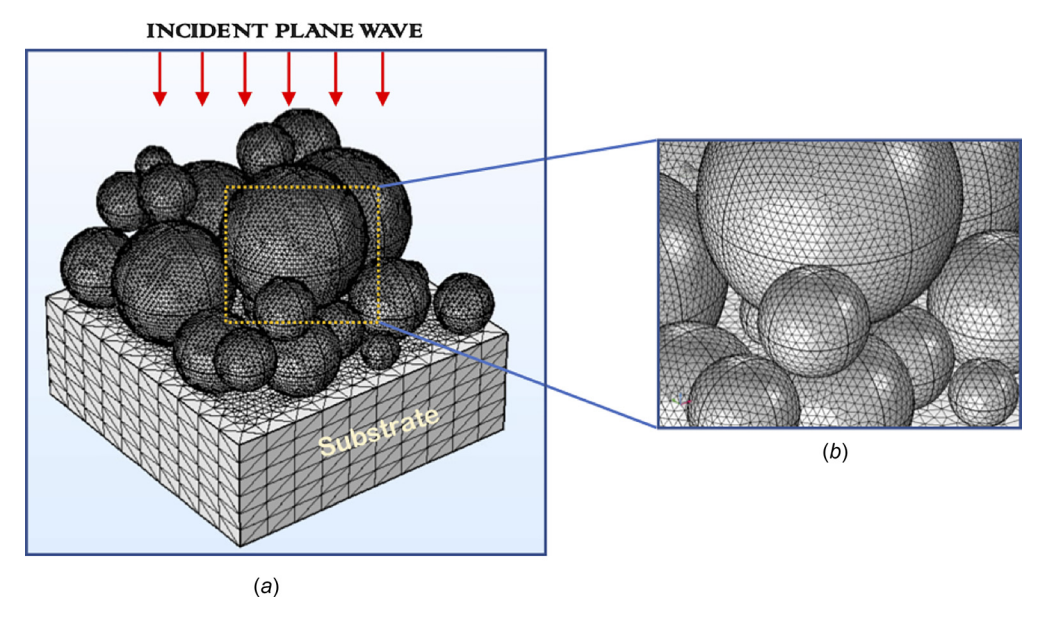


Fig. 2 Modeling approach: (a) typical nanoparticle packing distribution on a substrate $(1 \, \mu \text{m} \times 1 \, \mu \text{m})$ generated by using the DEM and (b) mesh setup for nanoparticle packing on a substrate

roughness and grain boundaries and can strongly influence nearfield radiative transport between nanoparticles, needs to be understood to characterize the micro/nanoscale thermal energy transport.

Finally, we note that the detailed structure of the nanoparticle packing can strongly influence light—material interactions under laser illumination. A discrete element method (DEM) is therefore used in this paper to create initial nanoparticle packings [26] for nanoparticle inks, which are observed experimentally; details are given in our earlier studies of heat transport and interfacial thermal conductance in physically plausible nanoparticle packing structures [27–30]. By selecting the thermal interfacial conductance ($G_{\rm IC}$) that enables the results of numerical thermal modeling to match the nanoparticle packing temperature, which is observed experimentally under laser irradiation, we are able to determine the primary modes of heat transfer. Thermal transport within the nanoparticle packing and the resulting temperature distribution are analyzed in detail.

2 Methods

2.1 Nanoparticle Packing Generation. Figure 1(a) shows a scanning electron micrograph of a copper nanoparticle distribution in a typical nanoparticle assembly. The particle size distribution measured using dynamic light scattering is shown in Fig. 1(b). From this distribution, the copper nanoparticles in this

assembly were determined to have a log-normal distribution with 116 nm mean radius and a 48 nm standard deviation. A model of the nanoparticle packing was then generated with this mean radius/standard deviation and a log-normal distribution using the DEM described in Ref. [27]. Since the nanoparticles in μ -SLS are spread in an ink, which minimizes the cohesive forces between particles, and then the ink allowed to dry to form the nanoparticle assembly, only gravitational forces on the particles were considered in the DEM. This type of DEM model has been shown to be an accurate representation of the actual nanoparticle packings generated in the μ -SLS process [28,29]. A finite element mesh of the particles, as shown in Fig. 2, and the air domain, which surrounds the nanoparticles and substrate, were then generated in order to create finite element model. Overall, four different nanoparticle packings were generated for this study in order to determine how the exact nanoparticle configuration affects the optical and thermal properties of the packing and to get a statistical distribution of the packing properties. Each packing contains approximately 22 particles.

2.2 Modeling Approach

2.2.1 Coupled Electromagnetic—Thermal Model for Laser Heating. A coupled electromagnetic—thermal model is developed to simulate the thermal evolution of the nanoparticle packing. The

model determines the thermal energy transport due to laser-nanoparticle interactions by taking into account the sizeand temperature-dependent electrical and thermophysical properties of the particles.

In this analysis, the optical interactions due to electromagnetic heat source in the coupled model are first analyzed by calculating the energy absorption efficiency of the randomly distributed nanoparticles packings [30,31] and the volumetric heat source due to laser–particle interactions is included in the thermal computations. A heat transfer model is then implemented to simulate the thermal interactions within the nanoparticle packing. A finite element analysis is applied to solve the coupled electromagnetic-heat transfer numerically by implementing an interfacial thermal resistance at the surface of each nanoparticle interface as boundary condition in COMSOL [32]. The mesh used for the coupled electromagnetic—thermal model employed about 4 million elements. Computations on coarser meshes indicate that the average nanoparticle packing temperature varies by about 0.1%.

Heat transfer is modeled by the unsteady diffusion equation for a stationary continuous wave laser source. This is valid since the laser duration is much longer than the electron-phonon relaxation time ($\sim 10 \, \mathrm{s}$ of picoseconds) and the effective thermal conductivity of the particles is modified to account for boundary scattering effects. After the resistive heating ($Q_{\mathrm{source},i}$) is calculated, it is used in the thermal model as the heat source within the volume of each particle. Furthermore, heat loss from each particle to the ambient by thermal radiative heat transfer is considered. The laser is assumed stationary in the laboratory frame, and therefore there is no convective term corresponding to laser motion. Furthermore, our interest is in steady-state temperature predictions. Consequently, volatilization of organic solvents, which occurs in the early phase of particle heat-up, need not be considered in the analysis.

The coupled electromagnetic-thermal model is expressed by

$$\frac{\partial H_i}{\partial t} + \nabla \cdot (-k_i \nabla T_i) = Q_{\text{source},i} \tag{1}$$

where i = 1...N (total number of particles), k is the thermal conductivity, H is the total enthalpy, and includes the sensible enthalpy as well the latent heat of fusion in the melt phase. The heat generation term is obtained as follows:

$$Q_{\text{heat}} = \text{Re}\{-\nabla \cdot S\} = (\sigma + \omega \varepsilon'')|E|^2 + \omega \mu''|H|^2$$
 (2)

where S is the Poynting vector, σ is electrical conductivity (S/m), ω is the angular frequency (1/s), ε'' is the imaginary permittivity (F/m) and μ'' is the imaginary permeability (Hy/m); all properties in Eq. (2) are considered temperature-independent. Equation (2) can be written in complex conjugate form as

$$Q_{\text{heat}} = \text{Re}\left[\left(\sigma E + j\omega D\right) \cdot E^* + j\omega B \cdot H^*\right]$$
 (3)

The heat generation term can then be calculated by

$$Q_{\text{source},i} = \frac{1}{2} \iiint_{V} \text{Re} \left[(\sigma E + j\omega D) \cdot E^* + j\omega B \cdot H^* \right] dV$$
 (4)

where * is the conjugate of the parameter. All simulations are performed at steady-state so that $(\partial H_i/\partial t)$ goes to zero.

The boundary conditions on the nanoparticle surface are

$$n \cdot k(\nabla T_{r_i})|_{\text{surface},i} = G_{IC}[T(r_i) - T_i]|_{\text{surface},i}$$
 (5)

$$n \cdot q_i = \varepsilon_i \sigma_b (T_i^4 - T_{\text{amb}}^4) \tag{6}$$

where i = 1...N and N is the total number of the nanoparticle in the structure, $G_{\rm IC}$ is the interfacial thermal conductance between

the nanoparticles, ε is the emissivity of the nanoparticles, σ_b is the Stefan-Boltzmann constant, and $T_{\rm amb}$ is the ambient temperature, which is taken as 293 K.

A periodic boundary condition $(-n_i \cdot q_i = n_o \cdot q_o)$ is applied at the sides of the domain, where q_i and q_o are the heat fluxes into and out of the boundaries. An insulated boundary condition $(n_b \cdot q_b = 0)$ is used at the bottom of the substrate; q_b is the outward-pointing heat flux from the substrate. The top boundary, which is far away from the nanoparticle surface, is taken as the ambient temperature, and is held at $T_{\rm amb} = 293$ K. The flowchart in Fig. 3 shows the coupling between the electromagnetic model and the thermal model.

2.2.2 Effect of Particle Size on Thermophysical Properties of Nanoparticles. Nanoparticles have been shown to have unique properties that are significantly different from bulk materials, resulting in part from their high surface to volume ratio. In this study, thermal conductivity, thermal conductance, and emissivity of copper nanoparticles are adjusted to account for size effects [33,34].

2.3 Experimental Analysis

2.3.1 Dynamic Scanning Calorimetry Experiment. In order to understand the thermal response of the nanoparticles, dynamic scanning calorimetry (DSC) measurement is conducted to measure the temperature where the onset of sintering and the melting of the nanoparticle inks occur [35]. Several nanoparticle inks are purchased from vendors (Intrinsiq Material, Rochester, NY, and Applied Nanotech, Austin, TX) and are tested in the DSC; however, only the "90 nm Cu ink for glass substrate" nanoparticle ink (green) is chosen for the laser sintering experiments in this study as shown in Fig. 4 due to its superior performance in the tests. While the vendor claims that this ink has a mean particle radius of 90 nm, when the mean particle radius is actually measured as in Sec. 2.1, the radius of the particles in this ink is determined to be log-normally distributed with a mean radius of 116 nm and a standard deviation of 48 nm. Therefore, this measured particle size distribution is used in the modeling analysis presented earlier.

Figure 4 depicts the heat flowrate (energy absorption rate per unit mass) versus the temperature of the nanoparticle ink. Three different nanoparticle inks are tested in the DSC: two nominally 90 nm Cu nanoparticle inks (Intrinsiq materials) designed for polyimide and glass substrates that have a thin polyvinylpyrrolidone (PVP) coating (<2 nm) on the nanoparticles to protect them from oxidation and an uncoated 100 nm Cu nanoparticle ink (Applied Nanotech). At about $175 \,^{\circ}\text{C} (\sim 450 \,\text{K})$, there is a sharp peak in the DSC curve that represents the decomposition of organic material for the two nominally 90 nm Cu nanoparticle inks. These organics are the residual solvent that is left on the nanoparticle surface after the drying process. Onset of particle necking is observed around 325 °C (~600 K) for uncoated 100 nm Cu nanoparticle ink but the sintering of the PVP coated inks does not occur until around 425 °C (~700 K) where there is a dip in the heat flowrate indicating the endothermic decomposition of the PVP coating followed by an increase in heat flowrate that represents the start of exothermic sintering between the particles.

2.3.2 Laser Experiment. Experiments are conducted to determine the sintering state of a copper nanoparticle packing on a substrate under the action of a solid-state continuous wave laser with a 532 nm central wavelength. The laser beam has a 3 mm waist diameter and is focused through a $50 \times (\text{NA-0.55})$ objective on to the nanoparticle packing with $50 \, \mu \text{m}$ spot size. A thermal power measurement sensor (Ophir optronics, 10A-P) and a photodiode sensor (Ophir optronics, PD 300) are used to measure the laser power. The laser power is adjusted between $3.0 \pm 1.4 \, \text{kW/cm}^2$ and $9.4 \pm 3.1 \, \text{kW/cm}^2$. Also, the thickness of the copper nanoparticle packing is measured as $0.4 \pm 0.2 \, \mu \text{m}$. Experiments are conducted at the University of Texas-at Austin with a collaboration work [36].

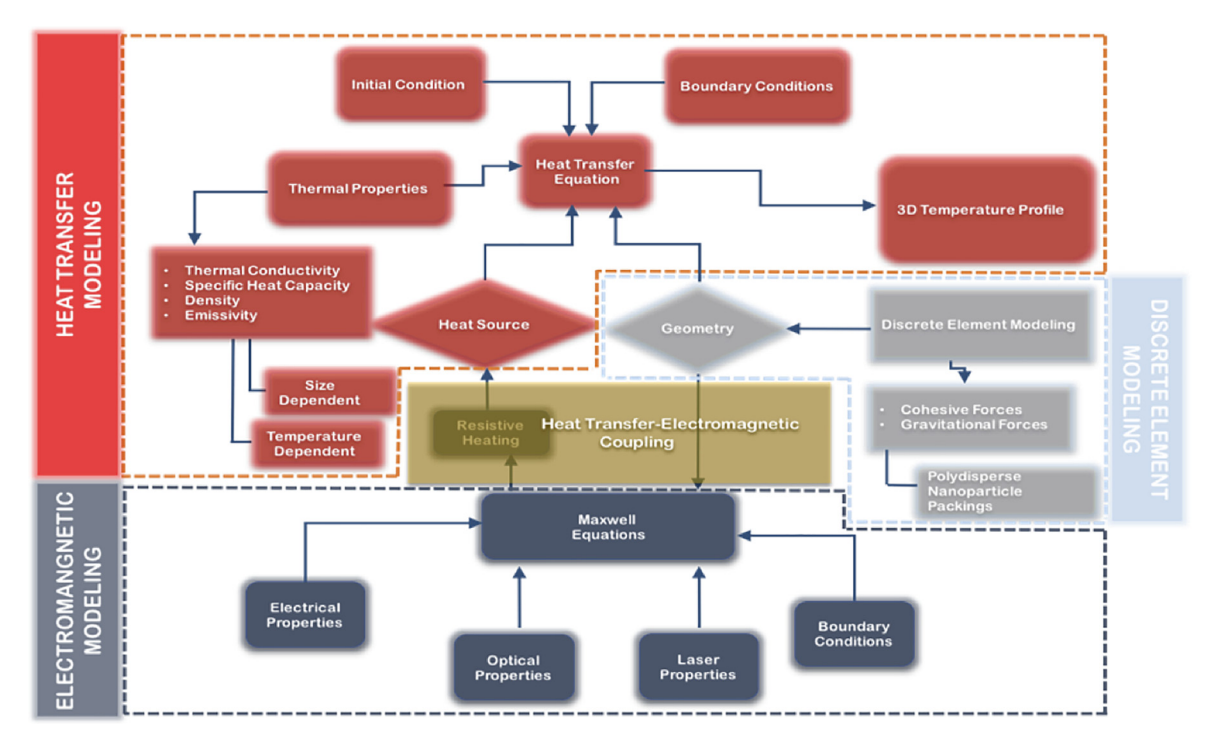


Fig. 3 Coupled electromagnetic and heat transfer model

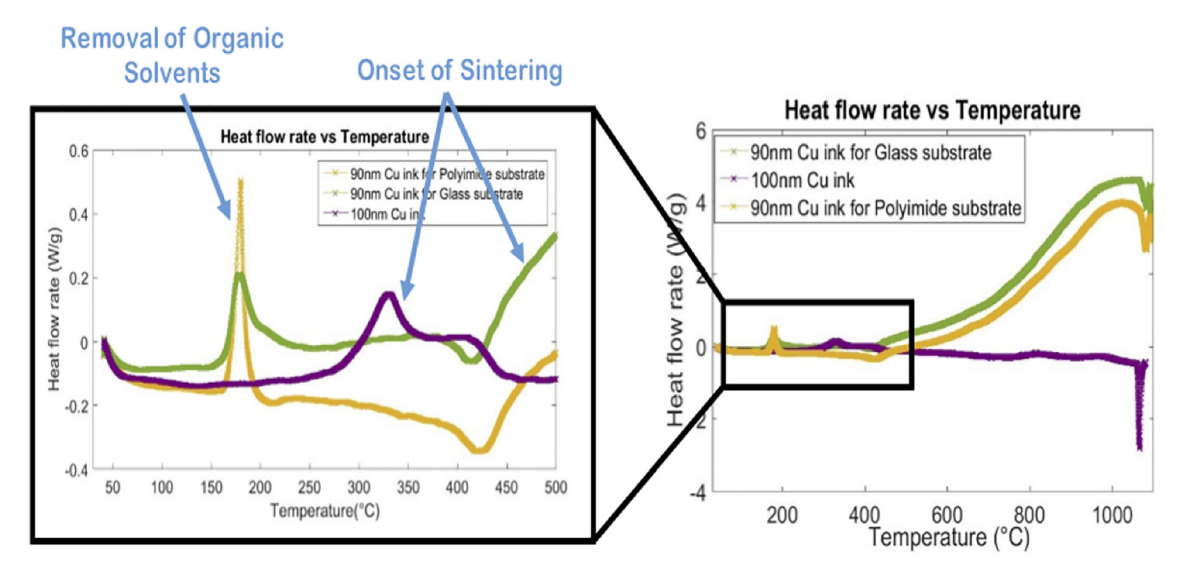


Fig. 4 Heat flowrate (energy absorption rate per unit mass) versus temperature of nanoparticle ink

As shown in Fig. 5, at longer exposure times ($\sim 500 \, \text{ms}$), sintering is seen to start when the laser power is at $\sim 2.5 \, \text{kW/cm}^2$. Weak sintering is observed when the laser power is $2.5 - 4 \, \text{kW/cm}^2$, good sintering is observed when the laser power is $4 - 7.5 \, \text{kW/cm}^2$, and melting is observed at laser power higher than $7.5 \, \text{kW/cm}^2$ for a $400 \, \text{nm}$ thick nanoparticle packing on a glass substrate.

3 Results and Discussion

3.1 Temperature Analysis of Nanoparticle Packings. In order to determine the temperature distribution of the particles in the nanoparticle assembly, both TE and TM polarized laser sources with 532 nm wavelength are applied to each of the four different particle packings described in Sec. 2. Due to space constraints, this section only presents results for one of the nanoparticle packings; the others are similar.

Overall, the interaction of the laser and the nanoparticle packing is complicated and has been discussed in previous papers [14,15,29,37]. As some particles in the assembly are closely packed together, near-field scattering enhances the optical intensity around these nanoparticles. Figure 6 shows the electric field intensity of copper nanoparticles on a glass substrate under 532 nm wavelength laser illumination.

The electric field intensity enhancement (I/I_0) is around 12–15 fold at a distance of $z=10\,\mathrm{nm}$ above the glass substrate for both the TE and TM polarizations, which I_0 is the calculated intensity of the laser source. However, the simulations for this nanoparticle packing show that the electric field intensity is around 140 for TE polarization and 107 for TM polarization at the contact points between touching particles and that the plasmonic interaction is strongest along the polarization direction. This shows that the plasmonic enhancement is a coupled function of both the laser

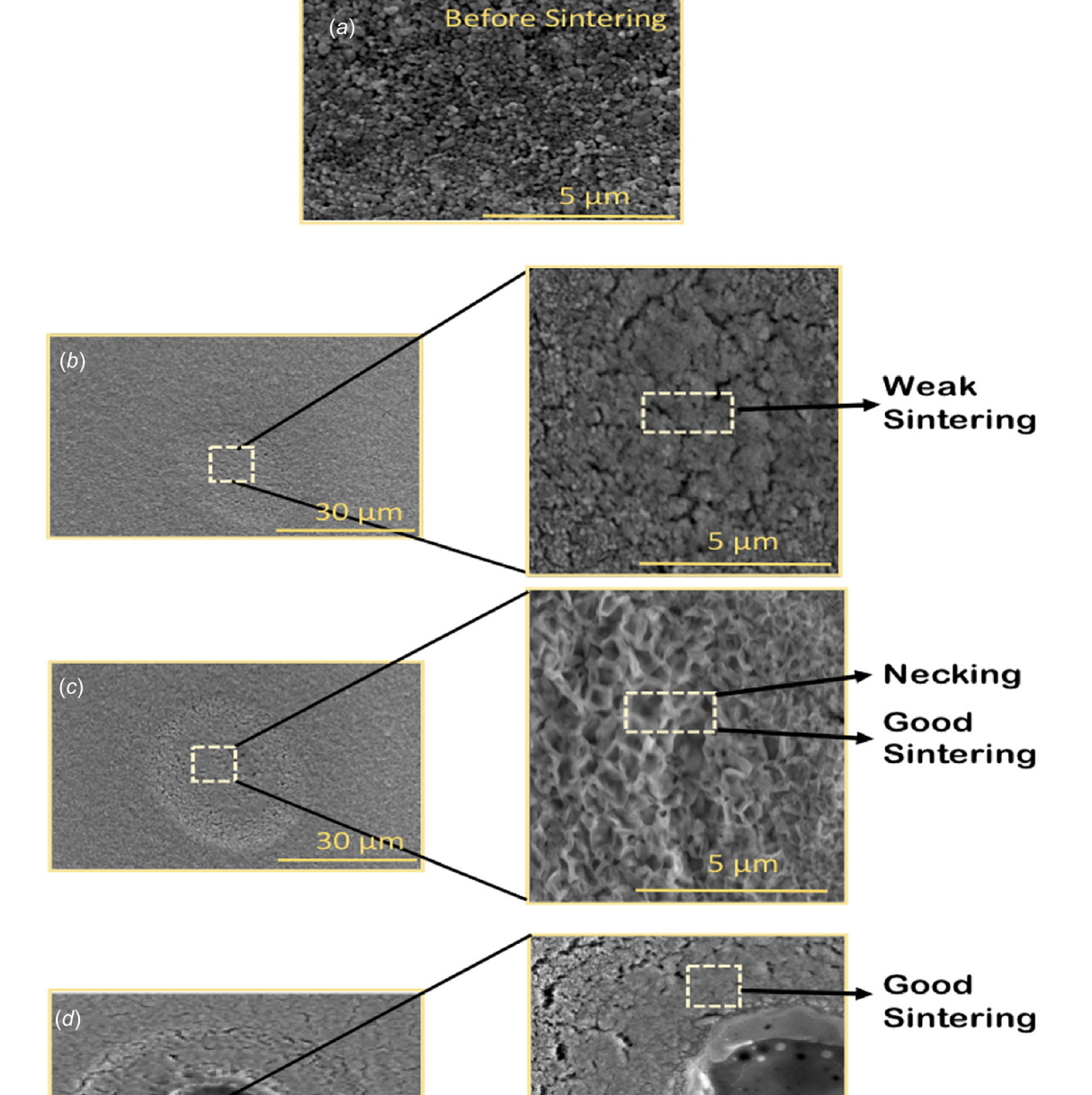


Fig. 5 Sintering experiments: SEM figures (a) particle distribution before sintering (b) $I = \sim 3 \, \text{kW/cm}^2$, (c) $I = \sim 6 \, \text{kW/cm}^2$, and (d) $I = \sim 9 \, \text{kW/cm}^2$ laser power

polarization and the nanoparticle configuration. For instance, at distance of 200 nm above the glass substrate, it is observed that two nanoparticle touching each other create a high electric field intensity. Due to the fact that these two particle cluster along the TM polarization direction, it is observed that the electric field intensity at the contact point is 140 for TE polarization but only 107 for TM polarization. This implies that the electric field intensity at the contact point can be significantly different for the TM and TE polarizations based on the exact particle configuration. However, the field enhancement is always largest at the contact point between two nanoparticles no matter the laser polarization. This suggests that the resistive heating of nanoparticles should be greatest near these contact points.

Figure 7 shows the resistive heating (W/m³) of one of the nanoparticle packings tested under varying laser power and polarization

In general, maximum resistive heating is found to increase linearly with increasing laser power for both polarizations. It is also observed that maximum resistive heating is higher along the polarization direction, which is expected due to the electric field enhancement along that direction. For a laser irradiation of $2.6\,\mathrm{kW/cm^2}$, the maximum resistive heating is around $4.9\times10^{16}\,\mathrm{W/m^3}$ for TM polarized irradiation, and is about 75% higher than the maximum resistive heating for TE polarized irradiation. This is due to the fact that a few small particles align well in the TM direction for this particle configuration. In general, smaller

Melting

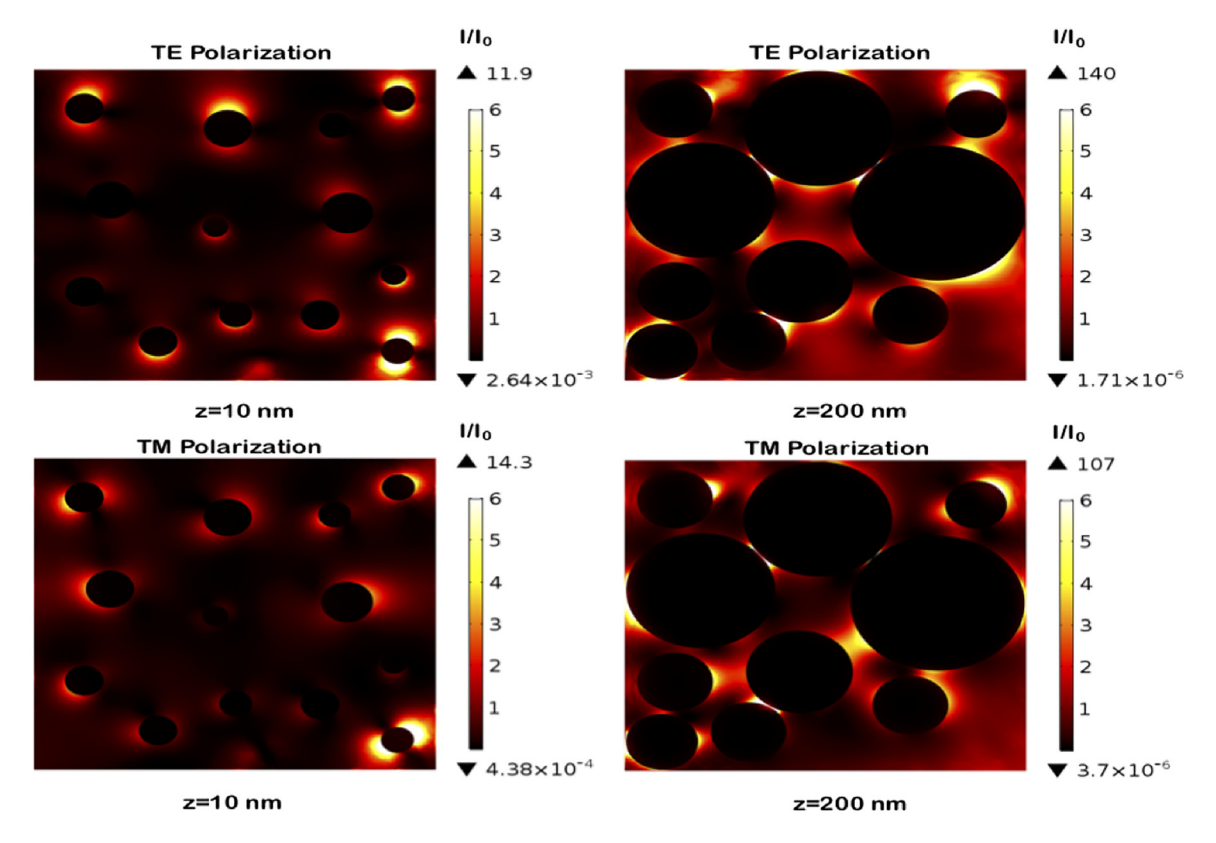


Fig. 6 Electric field intensity $(|II_0|)$ with a 532 nm laser with varying distance (z) above the glass substrate for a nanoparticle packing under TE and TM polarization

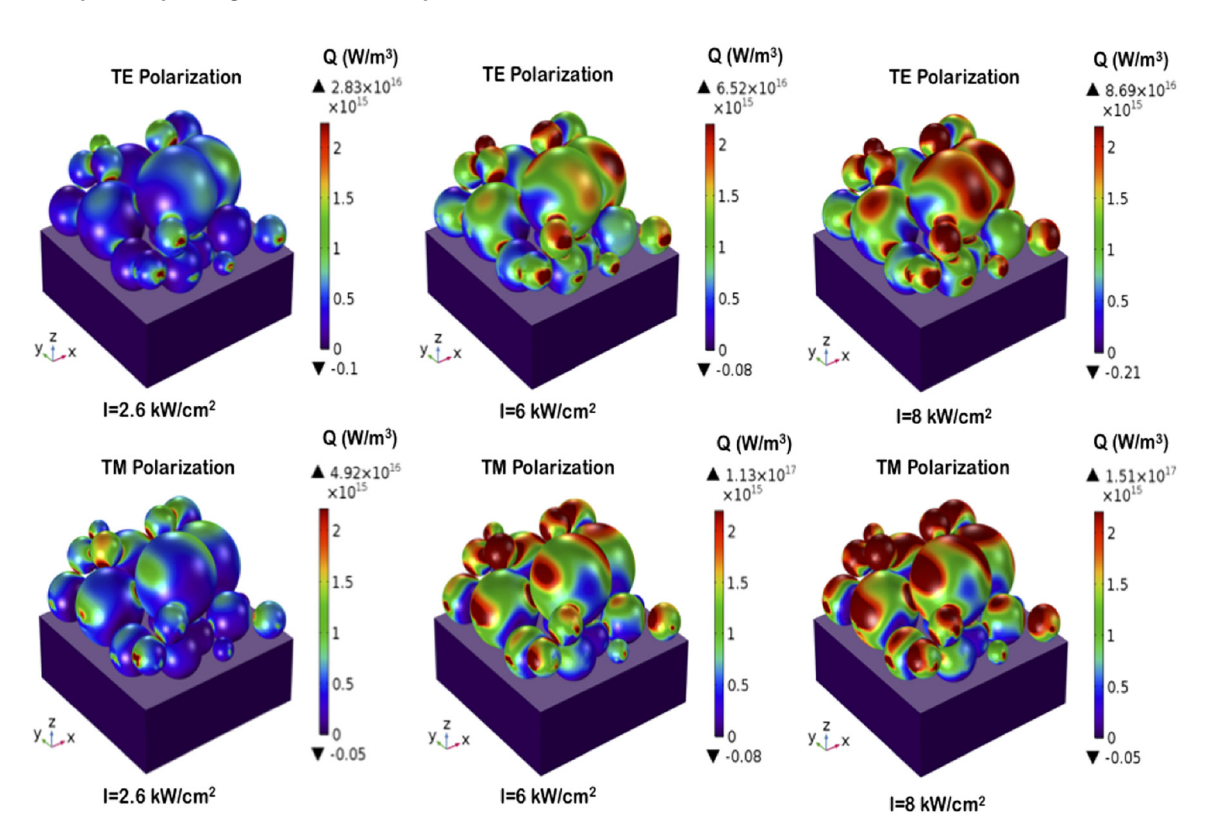


Fig. 7 Resistive heating (W/m³) of an example nanoparticle packing under varying laser power and polarization

particles result in greater resistive heating because of the greater field enhancement around the small particles although electrical conductivity decreases as the size of the nanoparticles decreases. However, depending on the exact

packing configuration, either TE or TM polarized irradiation may result in greater resistive heating. Therefore, multiple nanoparticle packings are tested in this analysis as shown in Sec 3.2.

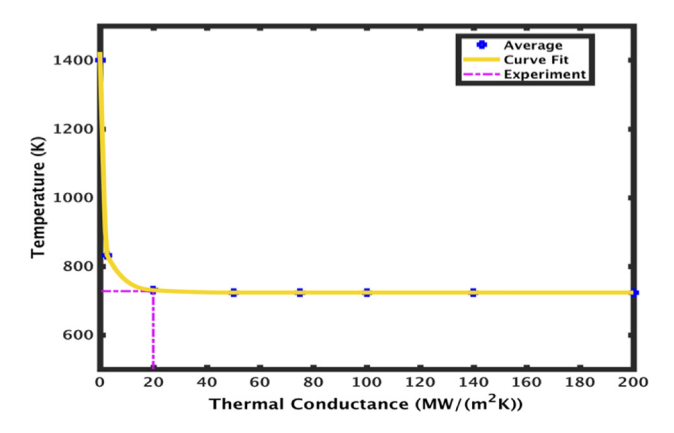


Fig. 8 Simulated average temperature versus interfacial thermal conductance for nanoparticle packing under $I = 2.6 \, \text{kW/cm}^2$ with TE and TM polarization

Once the resistive heating for each nanoparticle packing is determined, the coupled electromagnetic-heat transfer model can be solved with known interfacial thermal conductance between the particles. As the exact interfacial thermal conductance value is difficult to measure, it is varied in the simulation to match with the experimentally measured sintering temperature in this study. Figure 8 shows the simulated average temperature of the nanoparticle packings with various interfacial thermal conductance between the particles.

It is observed that when the interfacial thermal conductance is $20 \, \text{MW/m}^2 \text{K}$ and higher, it matches very well with experimentally observed sintering temperature. Thus, for all nanoparticle packings analyzed in this paper, the interfacial thermal conductance is assumed to be $20 \, \text{MW/m}^2 \text{K}$. This is also consistent with the literature [16,38,39].

The temperature distribution under 2.6 kW/cm² laser irradiation is shown in Figs. 9 and 10 for TE and TM polarizations, respectively. Figure 9 shows the temperature distribution on different cross section above a glass substrate (z) for the TE polarized laser. It is observed that some particles reach a maximum temperature of around 740 K. The difference between the maximum and minimum nanoparticle temperatures in the packing is found to be \sim 30 K. At 10 nm above the glass substrate, nanoparticle temperatures are in the 730–742 K range. At z = 200 nm, at the middle of the nanoparticle packing, the temperature is in the range 712–740 K. It can be observed from Fig. 9(c) that at the nanoparticle packing surface ($z = 400 \,\mathrm{nm}$), small nanoparticles sitting on top of the packing achieve the highest temperatures within the nanoparticle packing. The temperature between closely spaced nanoparticles is observed to be around 720 K, which implies that necking [40] between these particles should occur since the sintering temperature for these types of copper nanoparticles has previously been found to be \sim 700 K [35].

Figure 10 depicts the temperature distribution under TM polarization. It is observed that the temperature range is between 735 K and 750 K at a height of 10 nm above the glass substrate. Between 5 K and 8 K increase in temperature above that for the TE polarization is observed. Maximum and minimum temperatures of the nanoparticles in the packing are observed to be 750 and 735 K, respectively, at 10 nm above the substrate. At the middle of the nanoparticle packing ($z=200\,\mathrm{nm}$), the difference in the maximum and minimum particle temperature is observed to be around 30 K. This temperature variance is due to the fact that the distribution of nanoparticles within the assembly is random. Therefore, different particles interact differently with each polarization which creates local hot spots and causes each particle to reach a slightly different temperature.

Particle size can have a significant impact on the temperature of a particle since the field enhancement and resistive heating generally go up as the particle size goes down. For example, it is

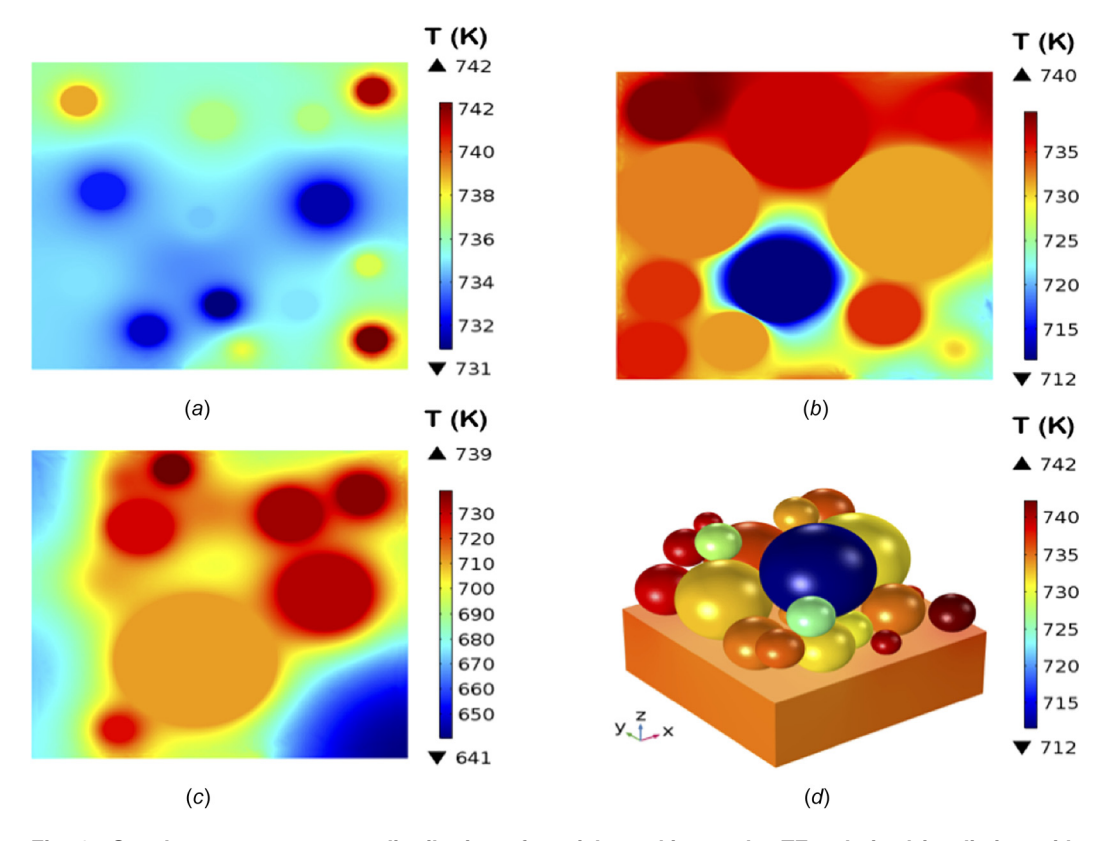


Fig. 9 Steady-state temperature distribution of particle packing under TE polarized irradiation with $I=2.6\,\mathrm{kW/cm^2}$. (a) Plane at $z=10\,\mathrm{nm}$ above glass substrate, (b) plane at $z=200\,\mathrm{nm}$, (c) plane at $z=400\,\mathrm{nm}$, and (d) oblique view.

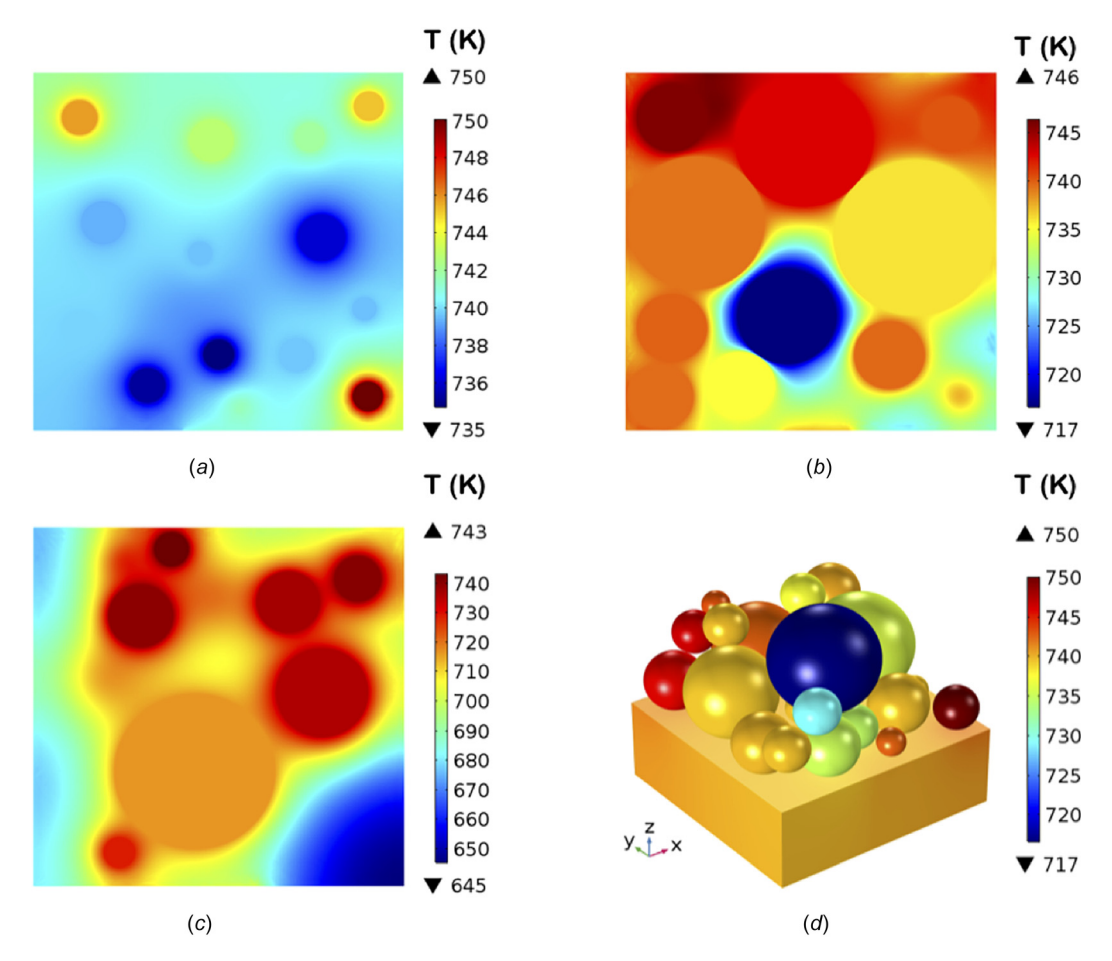


Fig. 10 Steady-state temperature distribution of particle packing under TM polarized irradiation with $I = 2.6 \text{ kW/cm}^2$. (a) Plane at z = 10 nm above glass substrate, (b) plane at z = 200 nm, (c) plane at z = 400 nm, and (d) oblique view.

observed from Fig. 10 that the particles smaller than the mean radius (116 nm) heat up more than the bigger particles, by up to 30-35 K. This creates hot spots, as seen in Fig. 10(b).

The present model does not consider how the change in morphology of the nanoparticles will affect the temperature distribution. In general, around 700 K, the copper nanoparticles will start to neck together. When this necking occurs, the contact area between the particles will increase, which will result in lower field enhancement and more conduction heat transfer. These changes are expected to reduce the temperature gradient across the packing in steady-state. More research need to be done in exploring the effects of the change in morphology due to sintering and melting. The present model is effective for predicting the onset of sintering, but does not yet address high laser power where such effects are expected to predominate.

3.2 Uncertainty Analysis and Comparison to Experimental Results. Since the exact particle arrangement can have a big impact on the near-field thermal energy transport between nanoparticles [14,15,29], four different particle packings are generated with the same particle size distribution to determine the effect of packing geometry on the temperature distribution. Figure 11 shows the particle packing geometries used in this study.

Figure 12 summarizes the temperature of the mass average (T_{average}) of the particles when different laser powers are used to heat the particles. Note that the melting of nanoparticles was not considered in this study since the μ -SLS process is a solid state sintering process, and as such, the computed results are not valid

when the nanoparticle packing temperature is above the melting point, However, the simulation should still give a good estimate of the temperature for low laser power. The error bars on temperature shown in Fig. 12 are obtained from simulations on the four particle packings shown in Fig. 11. We note that the variability in the average nanoparticle packing temperature is relatively small across the four packings, and is typically under 5%.

It is observed that nanoparticle packing temperature is linearly dependent on the laser power up until the melting point where this model is valid. The average temperature of the packings, $T_{\rm average}$, was found to be 730±3 K for a laser power of 2.6 kW/cm² and 1304±23 K for a laser power of 6 kW/cm², respectively. The median temperature of the particles $(T_{\rm median})$ within the nanoparticle packings for the 2.6 kW/cm² and 6 kW/cm² laser powers were found to be 735 ± 1 K and 1315 ± 7.5 K, respectively. Overall, the temperature of the particles within the packing follows a normal distribution as can be observed in Fig. 13. The laser polarization was found to have very little effect on the average nanoparticle packing temperature, as expected with randomly generated assemblies. For a laser power of 2.6 kW/cm², the massweighted particle temperature is observed to be 729±3.5 K and 731±2.5 K for the TE and TM polarizations, respectively. For a laser power of 6 kW/cm², the mass-weighted particle temperature is observed to be 1301±30.8 K and 1307±18.9 K for TE and TM polarizations, respectively. The maximum temperature difference between particles in the nanoparticle packing for the 2.6 kW/cm² laser source was found to be 40 K for the TE polarization and 44 K for the TM polarization. The maximum temperature difference between the particles in the nanoparticle packings for the

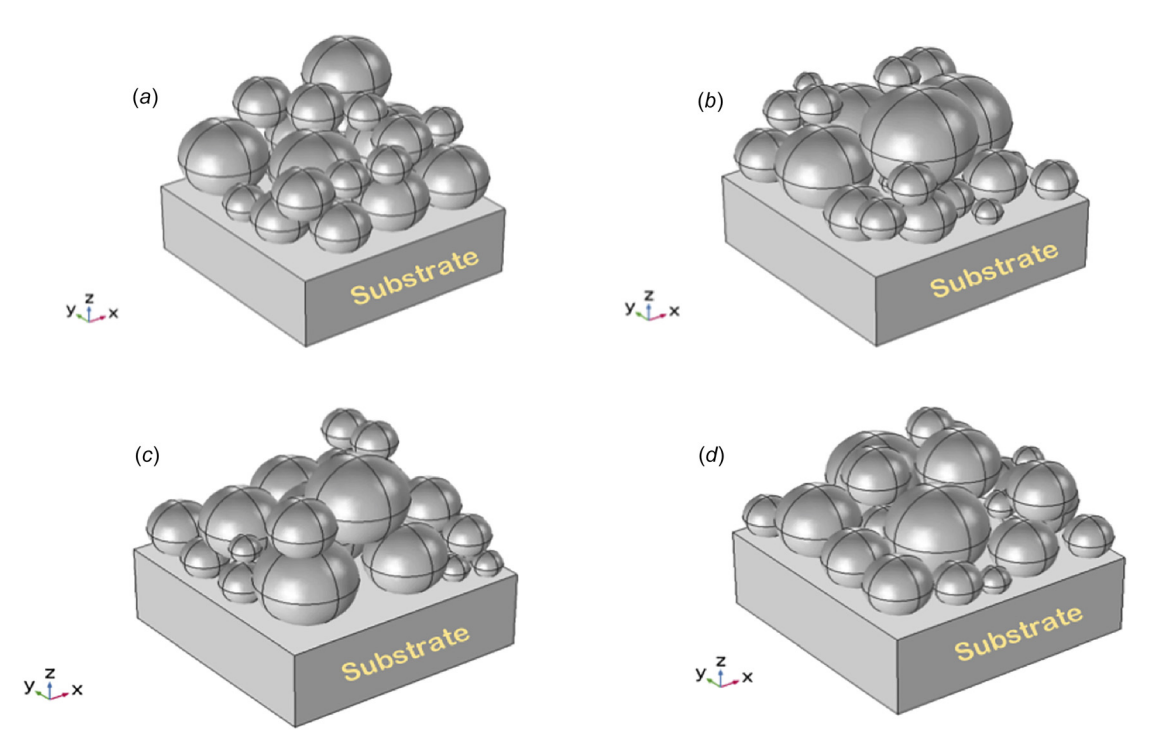


Fig. 11 Four copper nanoparticle packings generated for this study. The packings are log-normally distributed, with a 116 nm mean radius and 48 nm standard deviation. The final nanoparticle packing is about 400 nm thick and is located on a $350 \, \text{nm} \times 1000 \, \text{nm} \times 1000 \, \text{nm}$ substrate.

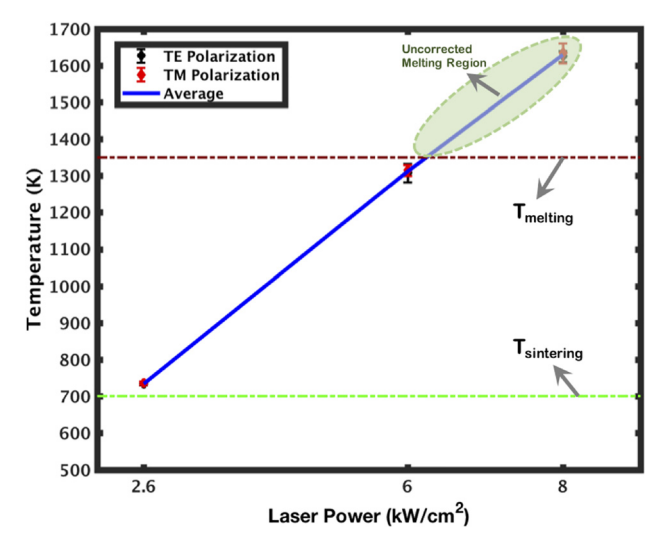


Fig. 12 Temperature distribution from coupled electromagnetic-heat transfer model under different laser power and polarization

 $6\,\mathrm{kW/cm^2}$ laser source was found to be 92 K and 100 K for TE and TM polarizations, respectively.

Figure 13 shows the particle temperature histogram based on the four different particle packing simulations illustrated in Fig. 11. It is shown that most particles are within 730 K–740 K temperature range for 2.6 kW/cm² laser power, which is very close to the experimentally observed onset of sintering temperature. For a laser power of 6 kW/cm², the simulation results predict that most of the copper nanoparticles will be within the temperature range of 1290 K–1330 K. Overall, these simulation predictions are in excellent agreement with experimental observations of laser induced copper nanoparticle sintering. Previous experimental results have shown that the onset of sintering of the type of

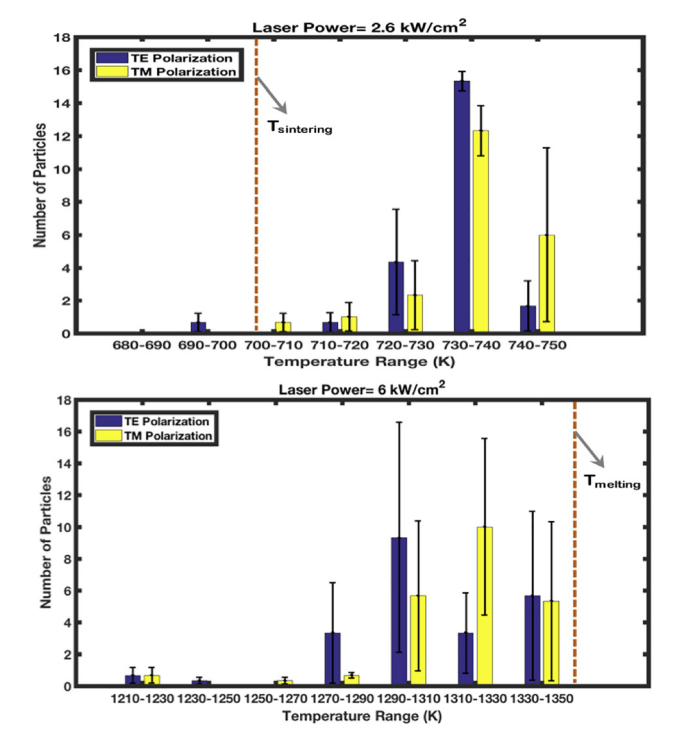


Fig. 13 Particle temperature histogram for different polarizations and laser powers

copper nanoparticles used in this study (CI-005 copper nanoparticle ink from Intrinsiq Materials, Inc.) occurs at around 700 K and the melting temperature of the copper nanoparticles is 1353 K [35]. It is also observed experimentally that copper nanoparticles in a 400 nm thick nanoparticle packing on a glass substrate start to neck and sinter together at laser powers of around 2.6 kW/cm²

and are well sintered at a laser power $6 \, kW/cm^2$. In addition, it has been observed that copper nanoparticle packings start to melt at laser powers of between 6 and $8 \, kW/cm^2$ [36]. Based on these experimental results, we would expect the temperature of the nanoparticles at a laser power of $2.6 \, kW/cm^2$ to be just above $700 \, K$, which is in good agreement with the simulation predictions of $730 \, K$. In addition, we would expect the nanoparticles to achieve their melting temperature of $1353 \, K$ at a laser power of between 6 and $8 \, kW/cm^2$, which also matches well with our predictions. For laser power higher than about $6 \, kW/cm^2$, phase change will need to be included in the modeling in order to observe such melting effects. However, based on these experimental observations, the coupled electromagnetic—thermal model does a very good job predicting the nanoparticle packing temperatures within the solid-state sintering region of interest to μ -SLS.

It is important to note that the nanoparticles used in the experiments have a few nanometers of polymer coating on them that prevents oxidization and agglomeration while the nanoparticles in the simulation are assumed to be pure copper. This coating could have an effect on thermo-optical properties of the nanoparticle packing. In the literature, the interfacial thermal conductance between pure nanoparticles has been observed to be in the range of $10-200\,\mathrm{MW/m^2K}$ [16]. For the model presented in this paper, the interfacial thermal conductance was assumed to be $20\,\mathrm{MW/m^2K}$ since this is consistent with the literature and the exact interfacial thermal conductance is difficult to measure. However, in order to validate the model presented in this paper, the sensitivity of the model to the assumed interfacial thermal conductance must be investigated.

There are also four main modes of heat transfer within the nanoparticle packing: (1) thermal conduction within each particle, (2) interfacial thermal conduction between particles, (3) thermal conduction between the particles through the air, and (4) thermal radiation between the particles. We estimate that thermal conductance within the particle is about three orders of magnitude greater than interfacial thermal conductance between the particles. Also, thermal conductance associated with heat transfer between the particles through the air is about an order of magnitude smaller than the interfacial thermal conductance between the particles for a $G_{\rm IC}$ value of 20 MW/m²K; it is estimated to play an increasing role for values lower than 20 MW/m²K. Furthermore, both nearfield and surface-to-surface thermal radiation are more than five orders of magnitude smaller than heat conduction between particles. Overall, for the range of parameters considered in this study, the most significant mode determinant of heat transfer through the nanoparticle packing is particle-to-particle conduction through the contact interface between the particles, $G_{\rm IC}$.

4 Conclusions

The coupled electromagnetic-thermal model results match very well with the experimental observations from the microscale selective laser sintering system. At a laser illumination of 2.6 kW/cm², the average temperature of the nanoparticle packing is estimated to be about 730 K, which is consistent with the sintering threshold estimated from experiments. At a laser illumination of 6 kW/cm², the average temperature of the nanoparticle packing is found to be about 1310 K, which is just below the melting point of copper nanoparticles and is consistent with the experimental measurements for this laser power on glass substrates. It is also found that the exact particle configuration does not have a large effect on the temperature distribution in the four particle packing configurations that are analyzed. Furthermore, the temperature variance within the nanoparticle packings is typically less than 5% of the overall average temperature. Furthermore, the most important determinant of heat transfer in the nanoparticle packing is found to be thermal conduction through the interfaces between particles. The magnitude of the heat transfer is found to be dominated by the interfacial thermal conductance constant, $G_{\rm IC}$. Overall, this model presented in this study provides a very useful foundation for modeling the thermal transport in microscale selective laser sintering in the submicron regime.

Acknowledgment

The authors would like to thank N. Roy for performing the nanoparticle tracking analysis experiments, SEM analysis, and the necessary data analysis needed to produce the particle size distribution presented in Fig. 1. The authors would also like to thank N. Roy for performing the DSC experiments and for help with the analysis and interpretation of the results presented in Sec. 2.3.1 and in Fig. 4. This analysis was useful for validating the analytical results illustrated in Fig. 12. Finally, the authors would like to thank O. Dibua and N. Roy for designing the sintering experimental setup, collecting the data, performing the analysis, and interpretation of these results including the SEM metrology for the laser experiment results presented in Sec. 2.3.2 and Fig. 5. These experiments were valuable for validating the laser power versus temperature results presented in Sec. 3.2.

Nomenclature

D = electric displacement field

E = electric field

 $G_{\rm IC} = \text{interfacial thermal conductance}$

H = total enthalpy

I = electric field intensity

 I_0 = intensity of laser source

k =thermal conductivity

n = normal

q = heat flux

 $Q_{\text{source},i} = \text{resistive heating}$

t = time

T =temperature

 $T_{\rm amb} = {\rm ambient \ temperature}$

S = Poynting vector

 $\varepsilon = \text{emissivity}$

 $\varepsilon'' = \text{imaginary permittivity}$

 $\mu'' = \text{imaginary permeability}$

 σ = electrical conductivity

 $\sigma_b = \text{Stefan-Boltzmann constant}, 5.67 \times 10^{-8} \, \text{W m}^{-2} \, \text{K}^{-4}$

 $\omega = angular frequency$

 $\nabla = \text{divergence}$

References

- [1] Ko, S. H., Pan, H., Grigoropoulos, C. P., Luscombe, C. K., Fréchet, J. M., and Poulikakos, D., 2007, "All-Inkjet-Printed Flexible Electronics Fabrication on a Polymer Substrate by Low-Temperature High-Resolution Selective Laser Sintering of Metal Nanoparticles," Nanotechnol., 18(34), p. 345202.
- [2] Hu, A., Guo, J. Y., Alarifi, H., Patane, G., Zhou, Y., Compagnini, G., and Xu, C. X., 2010, "Low Temperature Sintering of Ag Nanoparticles for Flexible Electronics Packaging," Appl. Phys. Lett., 97(15), p. 153117.
 [3] Roy, N., Yuksel, A., and Cullinan, M., 2016, "Design and Modeling of a Micro-
- [3] Roy, N., Yuksel, A., and Cullinan, M., 2016, "Design and Modeling of a Microscale Selective Laser Sintering System," ASME Paper No. MSEC2016-8569, V003T08A002.
- [4] Ahmmed, K. M., Grambow, C., and Kietzig, A. M., 2014, "Fabrication of Micro/Nano Structures on Metals by Femtosecond Laser Micromachining," Micromachines, 5(4), pp. 1219–1253.
- [5] Link, S., Burda, C., Nikoobakht, B., and El-Sayed, M. A., 2000, "Laser-Induced Shape Changes of Colloidal Gold Nanorods Using Femtosecond and Nanosecond Laser Pulses," J. Phys. Chem. B, 104(26), pp. 6152–6163.
- [6] Takami, A., Kurita, H., and Koda, S., 1999, "Laser-Induced Size Reduction of Noble Metal Particles," J. Phys. Chem. B, 103(8), pp. 1226–1232.
 [7] Mafuné, F., Kohno, J. Y., Takeda, Y., and Kondow, T., 2001, "Dissociation and
- Aggregation of Gold Nanoparticles Under Laser Irradiation," J. Phys. Chem. B, **105**(38), pp. 9050–9056.
- [8] Kelly, K. L., Coronado, E., Zhao, L. L., and Schatz, G. C., 2003, "The Optical Properties of Metal Nanoparticles: The Influence of Size, Shape, and Dielectric Environment," J. Phys. Chem. B, 107, pp. 668–677.
- [9] Ray, P. C., 2010, "Size and Shape Dependent Second Order Nonlinear Optical Properties of Nanomaterials and Their Application in Biological and Chemical Sensing," Chem. Rev., 110(9), pp. 5332–5365.
- [10] Yurkov, G. Y., Fionov, A. S., Koksharov, Y. A., Koleso, V. V., and Gubin, S. P., 2007, "Electrical and Magnetic Properties of Nanomaterials Containing Iron or Cobalt Nanoparticles," <u>Inorg. Mater.</u>, 43(8), pp. 834–844.
- [11] Noguez, C., 2007, "Surface Plasmons on Metal Nanoparticles: The Influence of Shape and Physical Environment," J. Phys. Chem. C, 111(10), pp. 3806–3819.

- [12] Quinten, M., Leitner, A., Krenn, J. R., and Aussenegg, F. R., 1998, "Electromagnetic Energy Transport Via Linear Chains of Silver Nanoparticles," Opt. Lett., 23(17), pp. 1331–1333.
- [13] Maier, S. A., Brongersma, M. L., Kik, P. G., and Atwater, H. A., 2002,
- "Observation of Near-Field Coupling in Metal Nanoparticle Chains Using Far-Field Polarization Spectroscopy," Phys. Rev. B, 65(19), p. 193408.

 [14] Yuksel, A., Cullinan, M., and Murthy, J., 2017, "Polarization Effect on Out of Plane Configured Nanoparticle Packing," ASME Paper No. MSEC2017-3075, V002T01A036.
- [15] Yuksel, A., Cullinan, M., and Murthy, J., 2017, "Thermal Energy Transport Below the Diffraction Limit in Close-Packed Metal Nanoparticles," ASME Paper No. HT2017-4968, V002T13A005.
- [16] Cahill, D. G., Ford, W. K., Goodson, K. E., Mahan, G. D., Majumdar, A., Maris, H. J., Merlin, R., and Phillpot, S. R., 2003, "Nanoscale Thermal Transport," J. Appl. Phys., 93(2), pp. 793-818.
- [17] Bulgakova, N. M., Stoian, R., Rosenfeld, A., Hertel, I. V., Marine, W., and Campbell, E. E. B., 2005, "A General Continuum Approach to Describe Fast Electronic Transport in Pulsed Laser Irradiated Materials: The Problem of Coulomb Explosion," Appl. Phys. A, 81(2), pp. 345-356.
- [18] Kanavin, A. P., Smetanin, I. V., Isakov, V. A., Afanasiev, Y. V., Chichkov, B. N., Wellegehausen, B., Nolte, S., Momma, C., and Tünnermann, A., 1998, "Heat Transport in Metals Irradiated by Ultrashort Laser Pulses," Phys. Rev. B, 57(23), pp. 14698-14703.
- [19] Ekici, O., Harrison, R. K., Durr, N. J., Eversole, D. S., Lee, M., and Ben-Yakar, A., 2008, "Thermal Analysis of Gold Nanorods Heated With Femtosecond Laser Pulses," J. Phys. D: Appl. Phys., 41(18), p. 185501.
- [20] Wang, Y., Ruan, X., and Roy, A. K., 2012, "Two-Temperature Nonequilibrium Molecular Dynamics Simulation of Thermal Transport Across Metal-Nonmetal Interfaces," Phys. Rev. B, 85(20), p. 205311.
- [21] Jiang, L., and Tsai, H. L., 2005, "Improved Two-Temperature Model and Its Application in Ultrashort Laser Heating of Metal Films," ASME J. Heat Transfer, **127**(10), pp. 1167–1173.
- [22] Pustovalov, V. K., 2005, "Theoretical Study of Heating of Spherical Nanoparticle in Media by Short Laser Pulses," Chem. Phys., 308(1–2), pp. 103-108.
- [23] Ho, J. R., Grigoropoulos, C. P., and Humphrey, J. A. C., 1995, "Computational Study of Heat Transfer and Gas Dynamics in the Pulsed Laser Evaporation of Metals," J. Appl. Phys., 78(7), pp. 4696-4709.
- [24] Evans, W., Prasher, R., Fish, J., Meakin, P., Phelan, P., and Keblinski, P., 2008, "Effect of Aggregation and Interfacial Thermal Resistance on Thermal Conductivity of Nanocomposites and Colloidal Nanofluids," Int. J. Heat Mass Transfer, **51**(5–6), pp. 1431–1438.
- [25] Timofeeva, E. V., Gavrilov, A. N., McCloskey, J. M., Tolmachev, Y. V., Sprunt, S., Lopatina, L. M., and Selinger, J. V., 2007, "Thermal Conductivity and Particle Agglomeration in Alumina Nanofluids: Experiment and Theory, Phys. Rev. E, 76(6), p. 061203.

- [26] Garg, R., Galvin, J., Li, T., and Pannala, S., 2012, "Open-Source MFIX-DEM Software for Gas-Solids Flows: Part I-Verification Studies," Powder Technol., 220, pp. 122-137.
- Yuksel, A., and Cullinan, M., 2016, "Modeling of Nanoparticle Agglomeration and Powder Bed Formation in Microscale Selective Laser Sintering Systems, Addit. Manuf., 12, pp. 204–215.
- Yuksel, A., Edward, T. Y., Cullinan, M., and Murthy, J., 2017, "Analysis of Near-Field Thermal Energy Transfer Within the Nanoparticles," SPIE Paper No. 10.1117/12.2274158.
- Yuksel, A., Edward, T. Y., Cullinan, M., and Murthy, J., 2019, "Effect of Particle Size Distribution on Near-Field Thermal Energy Transfer Within the Nanoparticle Packings," J. Photon. Energy, 9(03), p. 1.
- [30] Yuksel, A., Yu, E. T., Cullinan, M., and Murthy, J., 2018, "Heat Transfer Modeling of Nanoparticle Packings on a Substrate," ASME Paper No. IMECE2018-88642, V08BT10A050.
- [31] Yuksel, A., Edward, T. Y., Murthy, J., and Cullinan, M., 2017, "Effect of Substrate and Nanoparticle Spacing on Plasmonic Enhancement in Three-Dimensional Nanoparticle Structures," J. Micro Nano-Manuf., **5**(4),
- [32] COMSOL, 2012, "RF Module User's Guide," COMSOL, Burlington, MA.
- [33] Zhang, Z. M., 2007, Nano/Microscale Heat Transfer (No. Sirsi) i9780071436748), McGraw-Hill Education, New York.
- Warrier, P., and Teja, A., 2011, "Effect of Particle Size on the Thermal Conductivity of Nanofluids Containing Metallic Nanoparticles," Nanoscale Res. Lett., **6**(1), p. 247.
- [35] Roy, N. K., Yuksel, A., and Cullinan, M. A., 2015, " μ -SLS of Metals: Physical and Thermal Characterization of Cu-Nanopowders," Solid Freeform Fabrication Conference (SFF), Austin, TX, Aug. 10-12, pp. 7-9.
- [36] Roy, N. K., Dibua, O. G., Jou, W., He, F., Jeong, J., Wang, Y., and Cullinan, M. A., 2018, "A Comprehensive Study of the Sintering of Copper Nanoparticles Using Femtosecond, Nanosecond, and Continuous Wave Lasers," J. Micro Nano-Manuf., 6(1), p. 010903.
- Yuksel, A., Edward, T. Y., Cullinan, M., and Murthy, J., 2018, "Uncertainty Analysis of Near-Field Thermal Energy Transfer Within Nanoparticle Packing," 17th IEEE Intersociety Conference on Thermal and Thermomechanical Phenomena in Electronic Systems (ITherm), IEEE, SanDiego, CA, pp. 46-50.
- [38] Wilson, O. M., Hu, X., Cahill, D. G., and Braun, P. V., 2002, "Colloidal Metal Particles as Probes of Nanoscale Thermal Transport in Fluids," Phys. Rev. B, 66(22), p. 224301.
- [39] Merabia, S., Shenogin, S., Joly, L., Keblinski, P., and Barrat, J. L., 2009, "Heat Transfer From Nanoparticles: A Corresponding State Analysis," Proc. Natl. Acad. Sci., 106(36), pp. 15113-15118.
- [40] Dibua, O. G., Yuksel, A., Roy, N. K., Foong, C. S., and Cullinan, M., 2018, 'Nanoparticle Sintering Model: Simulation and Calibration Against Experimental Data," J. Micro Nano-Manuf., 6(4), p. 041004.